



CHORUS

This is the accepted manuscript made available via CHORUS. The article has been published as:

Pressure-driven symmetry transitions in dense m^2 ice

Zachary M. Grande, C. Huy Pham, Dean Smith, John H. Boisvert, Chenliang Huang, Jesse S. Smith, Nir Goldman, Jonathan L. Belof, Oliver Tschauner, Jason H. Steffen, and Ashkan Salamat

Phys. Rev. B **105**, 104109 — Published 17 March 2022

DOI: [10.1103/PhysRevB.105.104109](https://doi.org/10.1103/PhysRevB.105.104109)

Pressure driven symmetry transitions in dense H₂O ice

Zachary M Grande,¹ C. Huy Pham,² Dean Smith,^{1,3} John H Boisvert,¹ Chenliang Huang,¹ Jesse S Smith,³ Nir Goldman,² Jonathan L. Belof,² Oliver Tschauner,⁴ Jason H Steffen,¹ and Ashkan Salamat^{1,*}

¹*Department of Physics and Astronomy, University of Nevada Las Vegas, Las Vegas, Nevada 89154, USA*

²*Lawrence Livermore National Laboratory, 7000 East Ave., Livermore, California 94550, USA*

³*HPCAT, X-ray Science Division, Argonne National Laboratory, Argonne, Illinois 60439, USA*

⁴*Department of Geoscience, University of Nevada Las Vegas, Las Vegas, Nevada 89154, USA*

(Dated: March 1, 2022)

X-ray diffraction and Raman spectroscopy of H₂O (ice) structures are measured under static compression in combination with grain normalizing heat treatment via direct laser heating. We report the transition from cubic ice-VII to a structure of tetragonal symmetry, ice-VII_t at 5.1 ± 0.5 GPa. This is succeeded by the H-bond symmetrization transition occurring at a pressure of 30.9 ± 3 GPa. Both experimental observations are supported by simulated Raman spectra from Density Functional Theory quantum calculations. The transition to H-bond symmetrization is evidenced by the reversible emergence of its characteristic Raman mode and a 2.5-fold increase in bulk modulus, implying a significant increase in bonding strength.

I. INTRODUCTION

The pressure-temperature phase diagram of H₂O exhibits a remarkable number of polymorphic transitions^{1,2}. At low pressures, this complexity arises from steric rearrangements of hydrogen-bonded (H-bond) molecules, while the H–O–H bond angle and length remain almost constant. H-bonds are established through correlated disorder of the protons between adjacent oxygen atoms such that, at each moment, two protons and one oxygen form an H₂O molecule³. Condensed H₂O (ice) structures generally exhibit network-like topologies similar to those of silica and silicates⁴. The behavior of these ice phases is dominated by this H-bond network.

Above 2.1 GPa and 300 K, ice-VII is the stable crystalline phase of H₂O. However, rather than transforming into further dense packed networks of H-bonded structures with increasing pressure, the H-bond becomes gradually weaker⁵. In this case, the protons migrate to a symmetric position^{6,7}, resulting in a transition to a mixed covalent/ionic O–H bond in ice-X. This mechanism is observable through infrared (IR) spectroscopy as a gradual softening of the anti-symmetric O-H stretching vibration and its eventual disappearance observed above 60 GPa,^{8,9} combined with a stiffening of lower frequency lattice and librational modes¹⁰. The bond strength in the mixed covalent/ionically bonded ice-X should differ from the H-bonded regime of ice-VII, resulting in a significantly lower compressibility. While this fundamental change in O-H bond character is generally accepted, there remain large uncertainties on the phase boundary between ice-VII and ice-X, with reported transition pressures ranging from 40 GPa to above 120 GPa^{8,9,11–19}. This can have large ramifications for equation of state models and studies of planetary interiors, where precise knowledge of these physical properties are needed for accurate interpretation of astronomical observations^{20,21}.

The substantial range in claims for the transition pressure to ice-X is largely due to the gradual na-

ture of the transition which may have as many as two intermediate structures to facilitate the H-bond symmetrization^{11,14,16,18,22}. Proton nuclear magnetic resonance (or H NMR) experiments directly probe the local environment of the H-bond of water providing a more detailed model of the energy potential.¹⁸ The potential, which is widely agreed upon, starts from a double well in ice-VII and as the density is increased it is gradually deformed and the barrier becomes increasingly shallow allowing for the proton tunneling rate to increase. This delocalizes the proton and gives it an average position between the two wells. Calculations by Trybel *et al.*²³ have further explored such delocalization effects of the proton and how effective ionization of the water molecule can play a significant role in shaping the energy potential of the H-bond. Additionally, analysis of the bulk modulus during quasi-dynamic compression up to 180 GPa has been interpreted as showing transitions for ice-VII to disordered ice-VII' and then to a disordered ice-X' before the fully symmetrized ice-X.²²

Structural measurements (X-ray and neutron diffraction) have shown anomalies in the 10–14 GPa regime typically relating to proton/deuteron dynamics,^{11,14,16,24,25} which have been coined as the proton-disordered ice-VII' phase. However, until now these claims have lacked support from spectroscopic evidence. These claims are largely based on measurements that show deviations or features not accommodated by the presumed cubic structure for ice-VII; at least one such anomaly has been suggested to result from a tetragonal distortion¹⁴. Neutron diffraction studies on D₂O have shown that the deuterons occupy sites inconsistent with the present ice-VII model¹⁶ and, in the transition to ice-VIII at lower temperatures, the oxygen sites become disordered as well as the deuteron sites²⁶.

Exploring the structure of different isotopes of water-ice becomes even more complex because bond states in soft molecular compounds are strongly affected by the anisotropic strain that results from applying non-hydrostatic stress. Thus, the phase boundary into ice-

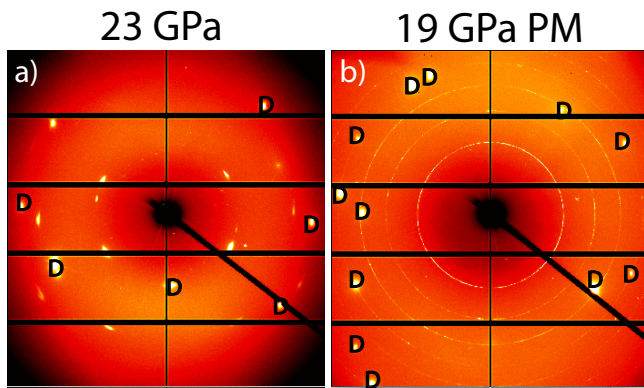


FIG. 1. **2-D X-ray diffraction images.** a) 2-D diffraction image of ice at 23 GPa with no heat treatment displaying high degree of texturing and broadening of multigrain peaks. b) 2-D diffraction image of ice at 19 GPa post melt (PM) showing full Debye-Scherrer rings for an extensive q -range with minimal broadening.

X may shift depending upon the nature of the non-hydrostatic stresses for a given experiment and on the length scale of a given diagnostic probe. $\text{H}_2\text{O}/\text{D}_2\text{O}$ measurements are especially susceptible to such conditions since using a pressure transmitting medium to establish hydrostatic equilibrium would contaminate the sample by formation of hydrates and clathrates. The resulting distortions are further exacerbated by the heterogeneous nucleation of ice-VII in ice-VI, which tends to produce large domains with a preferred orientation and create anisotropic strain and shearing at grain boundaries. This gives rise to significant texturing and broadening of Bragg peaks in X-ray diffraction (XRD)²⁷.

II. METHODS

Our observations support the occurrence of two pressure driven symmetry transitions in high pressure ice at room temperature below a megabar. These claims are supported by a combination of pressure-volume equation of state (EOS) measurements, Raman spectroscopy and density functional theory (DFT) calculations. Experimental compression data is acquired by using a diamond anvil cell (DAC) of custom design, driven by a gas membrane. Liquid H_2O (electrophoresis and spectroscopic grade; Sigma-Aldrich) is loaded into sample chambers formed by laser micromachining²⁸ accompanied by a $\sim 10 \mu\text{m}$ piece of polycrystalline Au to serve as a pressure marker. To avoid reactions between the heated H_2O and the Re gasket we line the inside of our sample chamber with Pt²⁹. We perform powder XRD at the HPCAT diffraction beamline (Sector 16-ID-B, Advanced Photon Source, Argonne National Laboratory, IL, USA) ($\lambda = 0.40663 \text{ \AA}$). Raman spectroscopy experiments are performed at UNLV using the same sample prepa-

ration technique. and a Ar-Kr laser lasing at 514.5 nm to excite the sample. We report spectroscopic data on the lattice modes of ice from 100 to 1000cm^{-1} but not the molecular stretching modes above 2000cm^{-1} due to overlap with the second order diamond signal at higher pressures.

In order to improve sample quality we utilize the high absorbance of ice in the mid-infrared to melt the ice sample and then let it cool back to ambient temperature. $10.6 \mu\text{m}$ radiation from a Synrad *Evolution*125 CO_2 laser is focused to a minimum spot size $\sim 30 \mu\text{m}$ and directly absorbed by the compressed sample, using an instrument built in-place at the diffraction beamline³⁰ or on a system housed at UNLV. Visible imaging confirms the melting and dynamic recrystallization of powdered ice²⁹. The cooling rate after melting is such that it promotes a normalized grain size and random orientation which is analogous to metallurgical normalization techniques³¹. The focused beam is translated throughout the sample chamber to make a homogeneous sample and relieving anisotropic strain from both the powdered ice and the Au pressure marker. The reduced domain sizes of the ice and their random orientations yield well-resolved Debye-Scherrer rings for an extensive q -range (Figure 1b), making our data suitable for Rietveld powder X-ray diffraction analysis. Data from samples that are not heat treated display significantly fewer diffraction features and typically exhibit multi-grain spots or highly textured rings with significant peak broadening from deviatoric strain. This is shown in Figure 1a and b where the FWHM of the (110) peak improves from 0.24 to $0.088^\circ 2\theta$ in the heat treated pattern. The powdered nature of the sample also reduces its susceptibility to further deviatoric strain as compression continues, despite the uniaxial nature of the DAC. The data quality is continuously improved by this heat treatment up to the final pressure measured in this experiment of 88 GPa and shows no evidence of chemical reaction or decomposition (Figure 1).

In addition, we perform quantum simulations of both ice-VII and ice-X using Kohn-Sham Density Functional Theory (DFT). Calculations were performed with the VASP code³², using the Perdew-Burke-Ernzerhof (PBE) generalized gradient approximation functional³³, and projector-augmented wave (PAW) pseudopotentials^{34,35}. We note that the PBE functional employed here is shown to yield good agreement with experimental results for ice properties at high pressure³⁶, particularly under the intense conditions of giant planetary interiors³⁷. We also found that functionals that include van der Waals interactions yield similar transition pressures from ice-VII to ice-X with the PBE functional²⁹. In this work, the relative Raman intensities for individual ice structures are determined from the derivative of the macroscopic dielectric tensor, computed from the finite-difference method with forwards and backwards displacements along each vibrational eigenmode³⁸. Please see the Supporting Information for additional details.

III. RESULTS

The onset of ice-VII is thus determined by heat treating immediately upon its coexistence with ice-VI (Supplementary Information). Control of pressure from the membrane-driven DAC allows incremental compression until the onset of phase coexistence is evident from XRD. The resulting sample comprises ice-VII only, giving an accurate determination of the starting volume, V_P , at the lower bound of its thermodynamic stability field. Only from 2.7 ± 0.4 GPa, can we unambiguously index and refine a single phase as cubic ice-VII. Above 5.1 ± 0.5 GPa, we observe deviations in the peak positions and profiles when fitting the XRD patterns to a cubic ice-VII model both before and – more clearly – after heat treating. This is most prominently shown by the Bragg feature at approximately 14.5° which displays splitting between the (200)/(002) which are not accommodated by the cubic ice-VII ($Pn\bar{3}m$) structure. Figure 2a shows the Bragg feature at $\sim 14.5^\circ$, where these deviations are most pronounced. Furthermore, a Bayesian analysis is applied to the unit cell data by examining the peak positions and profiles of all ~ 7 diffraction features observed and comparing the probability of a cubic structure against a tetragonal structure. The results of which strongly favor a tetragonal model above 5 GPa which we name here, ice-VII_t²⁹. We find that this transition from ice-VII to ice-VII_t is accompanied by a $2.18 \pm 0.01\%$ volume discontinuity of the unit cell at 5 GPa²⁹. The discrepancy in transition pressures between our tetragonal model and the previously named disordered ice VII' emphasize the influence of non-isotropic stress components in high-pressure experiments on ice as well as isotope effects^{11,14,16,24,25}.

We further investigate our observation of ice-VII_t by preparing new samples for Raman spectroscopy experiments, the results of which are consistent with the tetragonal structure above 5 GPa. We first observe the lattice modes of ice-VII near 3.3 GPa after heat treatment of the solidified sample (Figure 2b). This spectrum is dominated by a feature at 280 cm^{-1} fit to a single mode and also includes a weaker mode at 211 cm^{-1} (Figure 2b). Due to the close similarities between the Raman spectra of proton-disordered ice-VII and proton-ordered ice-VIII, these modes were previously assigned to the analogous translational-vibration modes of ice-VIII, B_{1g} and A_{1g} , respectively^{17,39}. We also observe a very weak mode which has not reported previously near 160 cm^{-1} ²⁹. Features were also observed in the 500 cm^{-1} to 800 cm^{-1} range corresponding to the known E_g and B_{2g} modes^{17,29}.

Beginning around 5.0 GPa, the dominant feature near 280 cm^{-1} displays an increasingly asymmetric profile. (Figure 2b, c and d). The appearance of new lattice modes (Figure 2c) is consistent with a lowering of symmetry from the cubic $Pn\bar{3}m$ space group to the tetragonal space group. We confirm this with our DFT calculations in Figure 2c, where the combined simulated Raman

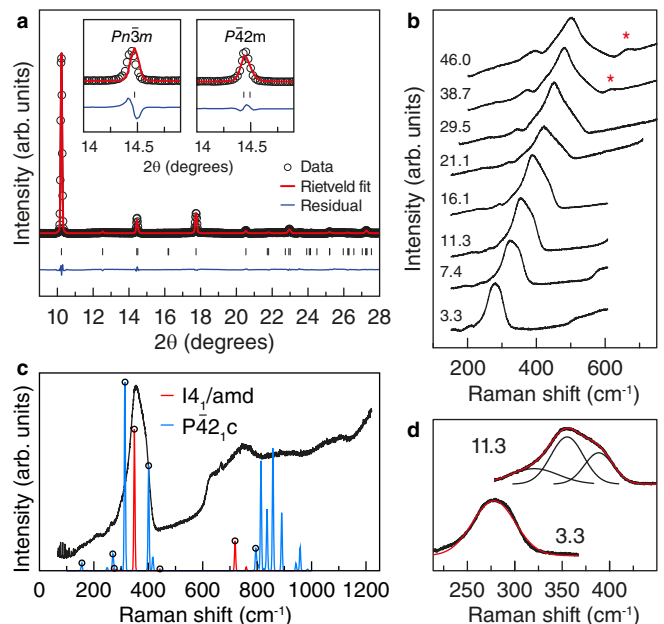


FIG. 2. **Evidence for ice-VII_t** **a** Rietveld refinement of ice-VII_t $P\bar{4}2m$ at 6.5 ± 0.5 GPa Inset: (left) Rietveld refinement of the (200) Bragg peak using a cubic cell ($Pn\bar{3}m$). (right) Improvement when using a tetragonal cell ($P\bar{4}2m$). **b** Progression of Raman features on increasing pressure. The dominant dominant mode near 280 cm^{-1} exhibits asymmetry above 5 GPa, and tends back to a single mode above 21 GPa. Red asterisks(*) denote the emergence of the ice-X T_{2g} Raman mode. **c** Simulated Raman spectra at 0K for two DFT computed ice-VII_t structures compared to the experimental spectra, both at approximately 10 GPa. **d** Dominant Raman feature of ice-VII at 3.3 GPa fit to a single peak whereas the feature in ice-VII_t at 11.3 GPa requires a triplet to fit in agreement with the simulated spectra.

spectra of two ice-VII configurations with body-centered tetragonal symmetry are needed to explain the broad feature centered at $\sim 280\text{ cm}^{-1}$ as well as the manifold of peaks above 700 cm^{-1} in the measurements. This supercell solution is required due to the partial occupancy of the hydrogen and oxygen sites, which is imperative in describing this phase of ice. The asymmetry of the observed experimental profile at 280 cm^{-1} is sustained until approximately 21.1 GPa, after which the peak profile becomes increasingly symmetric (Figure 2b).

We then map our DFT determined tetragonal supercells onto their single (two molecule) primitive unit cell in order to compare the DFT structure to our XRD data²⁹. This results in a space group of $P\bar{4}2m$ body-centered tetragonal structure that is equivalent to a slightly distorted ice-VII structure with non-cubic oxygen sites. Applying this tetragonal solution significantly improves the Rietveld refinement of our XRD data ($wR_P = 1.78\%$ and $R_P = 1.38\%$) to model our XRD data resulting in cell parameters $a = 3.2231 \pm 0.0002\text{ \AA}$ and $c = 3.2357 \pm 0.0003\text{ \AA}$ (Figure 2a inset), further supporting the presence of ice-VII_t.

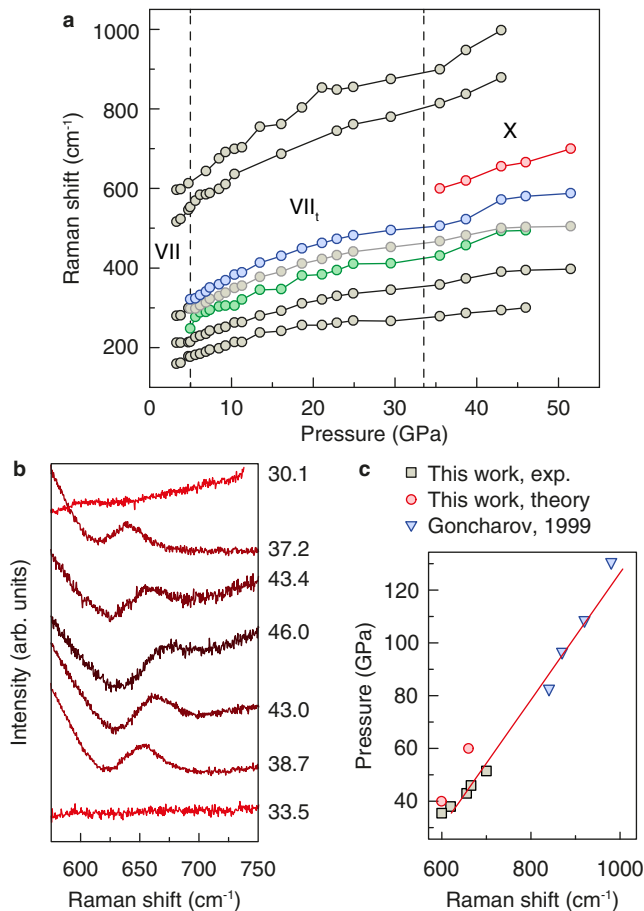


FIG. 3. **Raman spectrum of heat treated H₂O ices under compression.** **a** Frequency shift of measured Raman modes of H₂O ice with pressure. Splitting of the dominant lattice mode near 280 cm⁻¹ due to tetragonal distortion above 5 GPa is highlighted in blue and green. Red diamonds show the emergence of the ice-X T_{2g} mode above 33 GPa. Dashed lines represent transition pressures based on analysis of XRD data. **b** (bottom-to-top) Development of ice-X T_{2g} mode on compression above 33 GPa, and its reversible disappearance on decompression. **c** Frequency shift of ice-X T_{2g} Raman mode with pressure as determined by this study (experimentally and theoretically) and an interpolating line, as a guide, connecting to those reported by Goncharov *et al.*¹² at higher pressures.

By 38.7 GPa, a new feature is clearly observed in the Raman spectra of ice at 618 cm⁻¹ (Figure 3a and b), the intensity of which increases with pressure, and disappears upon decompression with little hysteresis (Figure 3b). We interpret this new mode as the T_{2g} mode, which signifies the onset of H-bond symmetrization in ice-X^{12,40}. The clear reversibility of the appearance/disappearance of this mode signals that this is a purely pressure driven phenomenon which is expected for the ice-X transition (Figure 3b). Furthermore, there is a noticeable stiffening of the frequency of the lattice modes, shown in Figure 3a, following the emergence of this new peak, in agreement with the significant mode strengthening which occurs at

the onset of ice-X. The blueshifting and broadening of librational and lattice modes due to symmetrization of the hydrogen bond is seen in a number of hydrides⁴¹, including water¹⁰.

Similar observations of the emergence of the T_{2g} mode previously confirmed the transition from ice-VIII to ice-X⁴⁰ at liquid nitrogen temperatures, albeit at a slightly shifted frequency from our measurements, as is expected from the temperature and density differences. Due to the aforementioned similarities between the Raman spectra of ice-VII and ice-VIII,^{17,39} this agreement supports our claim of a transition to the symmetric H-bonds at similar pressures.

We confirm our interpretation of the T_{2g} mode with DFT simulations of the ice-X Raman spectrum. The simulations show the appearance of a peak at close to 618 cm⁻¹ that is absent from all other simulated ice spectra in this study, including cubic ice-VII and ice-VIII. The frequency of this mode is tracked with pressure to 51.5 GPa and is in agreement with our computed Raman spectra and earlier measurements on ice-X made by Goncharov *et al.*¹² above 80 GPa as shown in Figure 3c.

The consistency in findings between the three independent tools used in this study (XRD, Raman spectroscopy, and DFT calculations) gives us confidence in our findings of a new crystal structure of tetragonal symmetry near 5 GPa and the onset of ice-X above 30 GPa. With this insight, we fit a three-phase P - V Vinet EOS to the data using Markov Chain Monte Carlo (MCMC). This model optimizes the EOS fit parameters based on the values obtained from least squares fitting²⁹ and also includes two transition pressures as fitting parameters. The results of our three-phase fit of the P - V EOS and the transition pressures as shown in Figure 4a. Our calculated transition pressure of ice-X at 30.9 ± 3 GPa (Figure 4a) corresponds well with the emergence of the T_{2g} mode in our Raman experiment as well as the discontinuity in bulk modulus shown in Méndez *et al.*²². Importantly, fitting of the region above 30.9 ± 3 GPa displays a 2.5X lowering in compressibility signifying a major change in the bonding character of ice.

In contrast, our DFT calculations (0 K structural optimization, with ions treated as classical particles) show a pressure transition from ice-VII to ice-X at ~ 90 GPa, in agreement with previous calculation studies⁴²⁻⁴⁴. However, it has been reported that the inclusion of the quantum nuclear vibrational effects on the nuclei can lower the transition pressure from the classical limit of 100 GPa to 30 GPa due to the proton being delocalized between the two sites on either side of the bond^{23,45,46}. This is consistent with our estimated experimental observation of the onset of ice-X at 30.9 GPa.

The validity of this three-phase model is best highlighted with the linearized form of the Vinet EOS relating the normalized pressure to Eulerian strain,⁴⁷ which is sensitive to the starting phase volume, V_0 . Using V_0 from a single-phase fit to ice-VII fails to describe the compressibility across the entire pressure range as seen by the ab-

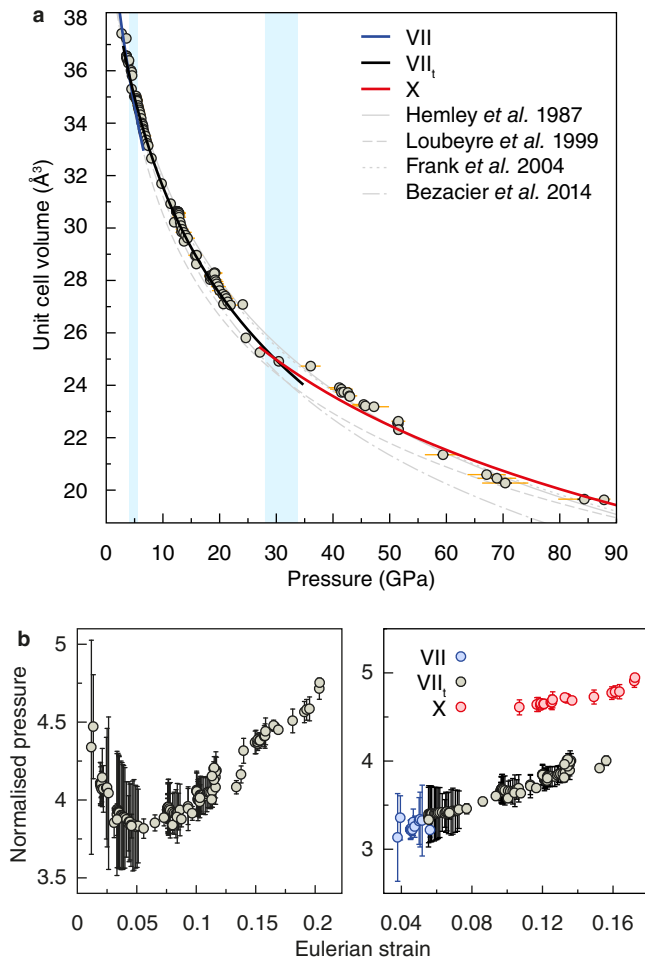


FIG. 4. **Equation of state fitting.** **a** Pressure-volume plot of our data and Vinet EOS fit from MCMC for the three phases. The calculated uncertainty in transition pressures are indicated by the blue shaded regions at 5.1 ± 0.5 GPa and 30.9 ± 2.9 GPa, respectively, and the grey lines are results from previous experiments. Curves are colour coded by phase (blue: cubic ice-VII black: non-cubic ice-VII_t and red: ice-X Orange error bars indicate our systematic uncertainty from deviatoric stresses in non heat treated data. **b** Linearized Vinet EOS. (left) When assuming a single phase model. (right) When assuming a three-phase model.

normal curvature in Figure 4b (left). Conversely, linear trends appear when modelling with three distinct phases and their fitted EOS parameters (Figure 4b (right)) signifying that the fit properly describes the P-V data.

IV. DISCUSSION AND CONCLUSION

The results of our multi-phase fit show that room temperature H₂O takes the form of cubic ice-VII as a single phase from 2.7 ± 0.4 to 5.1 ± 0.5 GPa, followed by tetragonal ice-VII_t to 30.9 ± 3 GPa, and the likely onset of H-bond symmetrization thereafter. These calculated phase

boundaries are reinforced by independent observations in our Raman spectroscopy study and DFT simulations. The low transition pressure into non-cubic ice-VII_t based on an observed lowering of symmetry and simulations, implies that cubic ice-VII is stable for only a small window of phase space – contrary to existing assumptions⁴⁸. Thus the ice-VII_t phase of ice could exist in abundance in the crust and upper mantle of expected water-rich super-earths.

Our results show a more than doubling of the bulk modulus of ice above 30 GPa which is validated by our analysis of the EOS fitting parameters in Figure 4b. This discontinuous change in bulk modulus with respect to pressure implies a phase transitions of at least third order or lower⁴⁹. A strong (2.5X) increase in bulk modulus signifies a dramatic increase in bond strength of the system⁵⁰. This increased bond strength is unlikely to be accommodated by the H-bonded network of ice-VII or ice-VII_t. This may be indicative of the onset of a stronger bonding taking place like a mix of covalent and ionic bonding which occurs in the H-bond symmetrization of the H₂O system.

The scattering power of hydrogen is too weak from X-ray diffraction techniques to provide sufficient quantifiable information on the hydrogen’s atomic position. Neutron crystallography is capable of accurately measuring the atomic positions in high pressure ice. However, these are limited to only studying deuterated samples, D₂O, as protons have a large incoherent scattering and negative scattering length. While measurements of D₂O are important, isotope effects in water are well known to shift transition lines. For example the shift in the transition line of ice-VI to VII⁵¹ at low pressures and it is likely to have an even stronger effect on the H-bond symmetrization pressure due to the doubled mass of the deuteron and quantum behavior of ice leading up to the transition.

Our Raman spectroscopy data shows a clear, reversible, transition at the same pressures as the XRD data. This implies a lower (1st or 2nd) order phase transition has taken place. We interpret this new mode as the T_{2g} mode, the only Raman active mode of ice-X. We confirm this by calculating the frequency for the T_{2g} mode at pressure and show they are in agreement with the measured frequency in Figure 3c. Furthermore, drawing an interpolating line between our measured pressure shift of the frequency with that of Goncharov *et al.*¹² shows a similar trend as seen in Figure 3c. However, we must acknowledge that the appearance of the T_{2g} mode does not coincide with the disappearance of the ice-VII_t modes. This is an unexpected result given that ice-X only has the single active raman mode. This result is also shown in previous measurements by Goncharov *et al.*¹² where the T_{2g} mode is shown with comparable intensity as the ice-VII_t raman modes past 80 GPa and only after approximately 94 GPa does the single ice-X mode dominate the presented spectra. This can be interpreted as possible phase coexistence but, our XRD data does not support

such a claim. Rather this is likely a sign of an intermediate state resulting from an effective centering of the proton due to tunneling effects before the collapse to a single well potential in fully ordered ice-X.

The studies on H₂O by Meier *et al.*¹⁸ and Trybel *et al.*²³ show that beginning as low as 20 GPa the protons exhibit a significant tunneling effect between the double well of the H-bond. This tunneling probability is shown to increase with pressure as the O—O distance decreases causing an effective centering in what they label ice X'. Our heat treatment technique improves our sample quality allowing us to observe this subtle transition by means of XRD and Raman scattering. These differ from the findings in neutron studies but we suspect these differences mostly arise due to the doubled mass of the deuteron, which significantly dampens tunneling effects, causing D₂O to behave more classically and pushing the H-bond symmetrization transition to a higher pressure than in H₂O. However, the disparity between our results and those of previous studies on H₂O is likely due to our alleviation of strain in the sample which may be an inhibitor to the transition to symmetric h-bonds. There is also the possibility that the other studies had contamination from an ionic species in their water samples which is shown to push the transition pressure of ice-X to higher pressures⁵².

We conclude that H₂O in the mixed ionic/covalent bond regime (ice-X or X') is 2.5X less compressible ($K_0 = 50.52 \pm 4.16$ GPa) than in the H-bond regime of ice-VII ($K_0 = 18.47 \pm 4.00$ GPa) and the newly reported ice-VII_t ($K_0 = 20.76 \pm 2.46$ GPa). These results require a significant redrawing of the high pressure phase diagram of ice as we show in Figure 5. The increased proton mobility which leads to the lower transition pressure to ice-X and ice-VII_t prior likely aids in the lower pressure transition to superionic ice phases at increased temperature⁵⁷. There is also a well-documented inflection in the melt line near 40 GPa^{53,54} shown in Figure 5 which has been associated with a density driven transition either above the melt line or below. In the case of below the melt line this would be associated with the transition to ice-X and we show this phase boundary in Figure 5. As our recorded transition pressure for ice-X is at much lower pressures than previous measurements the resulting Clapeyron slope for this transition is a steep positive slope contrary to prior beliefs.

The reversibility of the change in bonding states on the transition to ice-X makes a strong case for this to be a purely pressure driven transition. We expect this to diminish the thermodynamic driving force for the geochemical release of water in the Earth's crust and upper mantle at similar pressures, effectively trapping water in these physical regions. Although the pressure dependence of H-bond symmetrization in H₂O at high temperature remains to be studied, our discoveries provide a significant benchmark for continued advancements in understanding water at extreme conditions and its role in planetary interior processes.

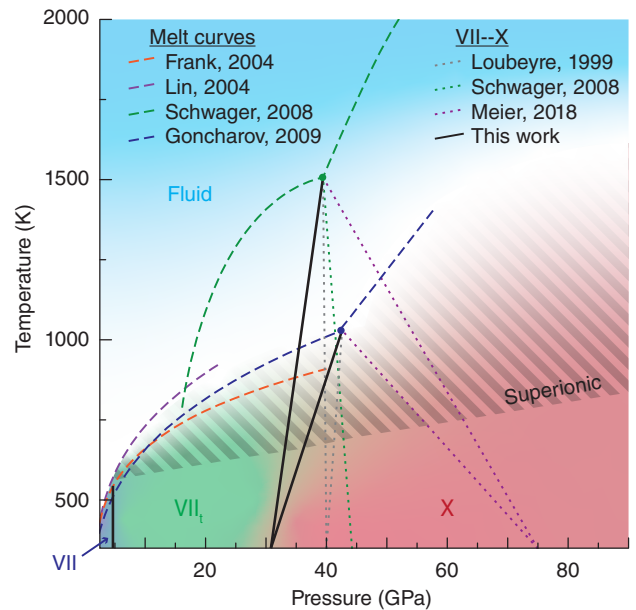


FIG. 5. **Phase Diagram of ice** Dark blue, green and red shaded regions denote ice-VII, VII_t and X, respectively, and projected phase boundaries separating high-pressure ice phases from our work are shown as solid black lines. Ice-X phase boundaries connect our measured transition at 30.91 ± 2.90 GPa and 300 K to the inflection point in the melt curve observed by Schwager and Boehler⁵³ and Goncharov *et al.*⁵⁴, which have been associated with the transition from molecular to ionic fluid. The same procedure has been used to project phase boundaries from Loubeyre *et al.*¹³ and Meier *et al.*¹⁸ In doing so, we deduce a steep, positive Clapeyron slope defining the transition from hydrogen bonding to ionic bonding in dense H₂O, consistent with a pressure-driven change in bonding nature. Dashed lines show measured melting curves.^{53–56} Superionic boundary from Sugimura *et al.*⁵⁷ is highlighted.

ACKNOWLEDGEMENTS

This research was sponsored in part by the National Nuclear Security Administration under the Stewardship Science Academic Alliances program through DOE Cooperative Agreement #DE-NA0001982. This work was performed at HPCAT (Sector 16), Advanced Photon Source (APS), Argonne National Laboratory. Lawrence Livermore National Laboratory is operated by Lawrence Livermore National Security, LLC, for the U.S. Department of Energy, National Nuclear Security Administration under Contract DE-AC52-07NA27344. J.S.S. acknowledge the support of DOE-BES/DMSE under Award DE-FG02-99ER45775. HPCAT operation is supported by DOE-NNSA under Award No. DE-NA0001974, with partial instrumentation funding by NSF. O.T acknowledges support from the National Science Foundation under award NSF-EAR 1838330. J.H.S. and J.H.B acknowledge support from NASA grants NNX16AK32G and NNX16AK08G. This research

made use of the Cherry Creek computer cluster admin-

istered by the UNLV National Supercomputing Institute.

-
- * salamat@physics.unlv.edu
- ¹ A. Dunaeva, D. Antsyshkin, and O. Kuskov, *Solar System Research* **44**, 202 (2010).
 - ² M. Millot, F. Coppari, J. R. Rygg, A. C. Barrios, S. Hamel, D. C. Swift, and J. H. Eggert, *Nature* **569**, 251 (2019).
 - ³ J. Li and D. Ross, *Nature* **365**, 327 (1993).
 - ⁴ R. M. Hazen, R. T. Downs, and L. W. Finger, *Science* **272**, 1769 (1996).
 - ⁵ K. Hirsch and W. Holzzapfel, *Physics Letters A* **101**, 142 (1984).
 - ⁶ W. Holzzapfel, B. Seiler, and M. Nicol, *J. Geophys. Res. Solid Earth* **89** (1984).
 - ⁷ F. H. Stillinger and K. S. Schweizer, *The Journal of Physical Chemistry* **87**, 4281 (1983).
 - ⁸ K. Aoki, H. Yamawaki, M. Sakashita, and H. Fujihisa, *Phys. Rev. B* **54**, 15673 (1996).
 - ⁹ A. Goncharov, V. Struzhkin, M. Somayazulu, R. Hemley, and H. Mao, *Science* **273**, 218 (1996).
 - ¹⁰ A. F. Goncharov, N. Goldman, L. E. Fried, J. C. Crowhurst, I.-F. W. Kuo, C. J. Mundy, and J. M. Zaug, *Phys. Rev. Lett.* **94**, 125508 (2005).
 - ¹¹ E. Wolanin, P. Pruzan, J. Chervin, B. Canny, M. Gauthier, D. Häusermann, and M. Hanfland, *Phys. Rev. B* **56**, 5781 (1997).
 - ¹² A. F. Goncharov, V. V. Struzhkin, H.-k. Mao, and R. J. Hemley, *Phys. Rev. Lett.* **83**, 1998 (1999).
 - ¹³ P. Loubeyre, R. LeToullec, E. Wolanin, M. Hanfland, and D. Hausermann, *Nature* **397**, 503 (1999).
 - ¹⁴ M. Somayazulu, J. Shu, C.-s. Zha, A. F. Goncharov, O. Tschauner, H.-k. Mao, and R. J. Hemley, *J. Chem. Phys.* **128**, 064510 (2008).
 - ¹⁵ E. Sugimura, T. Iitaka, K. Hirose, K. Kawamura, N. Sata, and Y. Ohishi, *Phys. Rev. B* **77**, 214103 (2008).
 - ¹⁶ M. Guthrie, R. Boehler, C. A. Tulk, J. J. Molaison, A. M. dos Santos, K. Li, and R. J. Hemley, *Proc. Natl. Acad. Sci. U.S.A.* **110**, 10552 (2013).
 - ¹⁷ C.-S. Zha, J. S. Tse, and W. A. Bassett, *J. Chem. Phys.* **145**, 124315 (2016).
 - ¹⁸ T. Meier, S. Petitgirard, S. Khandarkhaeva, and L. Dubrovinsky, *Nat. Commun.* **9**, 2766 (2018).
 - ¹⁹ M. Guthrie, R. Boehler, J. Molaison, B. Haberl, A. dos Santos, and C. Tulk, *Phys. Rev. B* **99**, 184112 (2019).
 - ²⁰ M. French, M. P. Desjarlais, and R. Redmer, *Phys. Rev. B* **93**, 022140 (2016).
 - ²¹ C. Huang, D. R. Rice, Z. M. Grande, D. Smith, J. S. Smith, J. H. Boisvert, O. Tschauner, A. Salamat, and J. H. Steffen, *Monthly Notices of the Royal Astronomical Society* **503**, 2825 (2021).
 - ²² A. S. J. Méndez, F. Trybel, R. Husband, G. Steinle-Neumann, H.-P. Liermann, and H. Marquardt, *Physical Review B* **103**, 064104 (2021).
 - ²³ F. Trybel, M. Cosacchi, T. Meier, V. M. Axt, and G. Steinle-Neumann, *Physical Review B* **102**, 184310 (2020).
 - ²⁴ T. Okada, T. Iitaka, T. Yagi, and K. Aoki, *Sci. Rep.* **4**, 5778 (2014).
 - ²⁵ R. Nelmes, J. Loveday, W. Marshall, G. Hamel, J. Besson, and S. Klotz, *Physical review letters* **81**, 2719 (1998).
 - ²⁶ K. Komatsu, S. Klotz, S. Machida, A. Sano-Furukawa, T. Hattori, and H. Kagi, *Proceedings of the National Academy of Sciences* **117**, 6356 (2020).
 - ²⁷ D. Balzar and H. Ledbetter, *J. Appl. Crystallogr.* **26**, 97 (1993).
 - ²⁸ R. Hrubiak, S. Sinogeikin, E. Rod, and G. Shen, *Rev. Sci. Instrum.* **86**, 072202 (2015).
 - ²⁹ See Supplemental Information at [URL will be inserted by the production group] for further experimental details and information on all calculations performed. Which includes Ref.⁵⁸⁻⁷² therein.
 - ³⁰ D. Smith, J. S. Smith, C. Childs, E. Rod, R. Hrubiak, G. Shen, and A. Salamat, *Rev. Sci. Instrum.* **89**, 083901 (2018).
 - ³¹ K.-E. Thelning, *Steel and its heat treatment* (Butterworth-Heinemann, 2013).
 - ³² G. Kresse and J. Hafner, *Phys. Rev. B* **47**, 558 (1993).
 - ³³ J. P. Perdew, K. Burke, and M. Ernzerhof, *Phys. Rev. Lett.* **77**, 3865 (1996).
 - ³⁴ P. E. Blöchl, *Phys. Rev. B* **50**, 17953 (1994).
 - ³⁵ G. Kresse and D. Joubert, *Phys. Rev. B* **59**, 1758 (1999).
 - ³⁶ M. Millot, S. Hamel, J. R. Rygg, P. M. Celliers, G. W. Collins, F. Coppari, D. E. Fratanduono, R. Jeanloz, D. C. Swift, and J. H. Eggert, *Nat. Phys.* **14**, 297 (2018).
 - ³⁷ M. Frenc, T. R. Mattsson, N. Nettelmann, and R. Redmer, *Phys. Rev. B* **79**, 054107 (2009).
 - ³⁸ A. Fonari and S. Stauffer, *vasp_raman.py* (<https://github.com/raman-sc/VASP/>, 2013).
 - ³⁹ P. Pruzan, J. Chervin, and M. Gauthier, *EPL (Europhysics Letters)* **13**, 81 (1990).
 - ⁴⁰ K. Hirsch and W. Holzzapfel, *J. Chem. Phys.* **84**, 2771 (1986).
 - ⁴¹ N. Goldman and L. E. Fried, *J. Chem. Phys.* **125**, 044501 (2006).
 - ⁴² M. Bernasconi, P. Silvestrelli, and M. Parrinello, *Phys. Rev. Lett.* **81**, 1235 (1998).
 - ⁴³ L. Tian, A. I. Kolesnikov, and J. Li, *J. Chem. Phys.* **137**, 204507 (2012).
 - ⁴⁴ X. Z. Lu, Y. Zhang, P. Zhao, and S. J. Fang, *J. Phys. Chem. B* **115**, 71 (2011).
 - ⁴⁵ M. Benoit, D. Marx, and M. Parrinello, *Nature* **392**, 258 (1998).
 - ⁴⁶ Y. Bronstein, P. Depondt, F. Finocchi, and A. M. Saitta, *Phys. Rev. B* **89**, 214101 (2014).
 - ⁴⁷ R. J. Angel, *Rev. Mineral. Geochem.* **41**, 35 (2000).
 - ⁴⁸ W. Holzzapfel, *J. Chem. Phys.* **56**, 712 (1972).
 - ⁴⁹ G. Jaeger, *Archive for history of exact sciences* **53**, 51 (1998).
 - ⁵⁰ M. Born and K. Huang, *Dynamical theory of crystal lattices* (Clarendon press, 1954).
 - ⁵¹ C. W. Pistorius, E. Rapoport, and J. Clark, *The Journal of Chemical Physics* **48**, 5509 (1968).
 - ⁵² L. E. Bove, R. Gaal, Z. Raza, A.-A. Ludl, S. Klotz, A. M. Saitta, A. F. Goncharov, and P. Gillet, *Proceedings of the National Academy of Sciences* **112**, 8216 (2015).

- ⁵³ B. Schwager and R. Boehler, *High Pressure Research* **28**, 431 (2008).
- ⁵⁴ A. F. Goncharov, C. Sanloup, N. Goldman, J. C. Crowhurst, S. Bastea, W. Howard, L. E. Fried, N. Guignot, M. Mezouar, and Y. Meng, *J. Chem. Phys.* **130**, 124514 (2009).
- ⁵⁵ M. R. Frank, Y. Fei, and J. Hu, *Geochimica et Cosmochimica Acta* **68**, 2781 (2004).
- ⁵⁶ J.-F. Lin, B. Militzer, V. V. Struzhkin, E. Gregoryanz, R. J. Hemley, and H.-k. Mao, *J. Chem. Phys.* **121**, 8423 (2004).
- ⁵⁷ E. Sugimura, T. Komabayashi, K. Ohta, K. Hirose, Y. Ohishi, and L. S. Dubrovinsky, *J. Chem. Phys.* **137**, 194505 (2012).
- ⁵⁸ R. Hemley, A. Jephcoat, H. Mao, C. Zha, L. Finger, and D. Cox, *Nature* **330**, 737 (1987).
- ⁵⁹ B. Kamb and B. L. Davis, *Proc. Natl. Acad. Sci. U.S.A.* **52**, 1433 (1964).
- ⁶⁰ J.-L. Kuo, J. V. Coe, S. J. Singer, Y. B. Band, and L. Ojamäe, *J. Chem. Phys.* **114**, 2527 (2001).
- ⁶¹ J.-L. Kuo and S. J. Singer, *Physical Review E* **67**, 016114 (2003).
- ⁶² J. D. Bernal and R. H. Fowler, *J. Chem. Phys.* **1**, 515 (1933).
- ⁶³ G. Kresse and J. Hafner, *Phys. Rev. B* **49**, 14251 (1994).
- ⁶⁴ G. Kresse and J. Furthmüller, *Comput. Mater. Sci.* **6**, 15 (1996).
- ⁶⁵ G. Kresse and J. Furthmüller, *Phys. Rev. B* **54**, 11169 (1996).
- ⁶⁶ J. P. Perdew, K. Burke, and M. Ernzerhof, *Phys. Rev. Lett.* **78**, 1396 (1997).
- ⁶⁷ H. J. Monkhorst and J. D. Pack, *Phys. Rev. B* **13**, 5188 (1976).
- ⁶⁸ N. Goldman, E. J. Reed, and L. E. Fried, *J. Chem. Phys.* **131**, 204103 (2009).
- ⁶⁹ B. Santra, J. Klimeš, A. Tkatchenko, D. Alfè, B. Slater, A. Michaelides, R. Car, and M. Scheffler, *The Journal of chemical physics* **139**, 154702 (2013).
- ⁷⁰ D. Foreman-Mackey, D. W. Hogg, D. Lang, and J. Goodman, *Publications of the Astronomical Society of the Pacific* **125**, 306 (2013).
- ⁷¹ J. H. Boisvert, B. E. Nelson, and J. H. Steffen, *Mon. Not. R. Astron. Soc.* **480**, 2846 (2018).
- ⁷² S. Dorfman, V. Prakapenka, Y. Meng, and T. Duffy, *Journal of Geophysical Research: Solid Earth* **117** (2012).